Bioactive Materials 50 (2025) 232–245

Contents lists available at ScienceDirect

Bioactive Materials

journal homepage: www.keaipublishing.com/en/journals/bioactive-materials

A multifunctional trap-capture-kill antibacterial system for enhanced wound healing via modified decellularized mushroom aerogels

Chuwei Zhang [a,b,1], Shuai Fan [c,1], Jing Zhang [d,1], Ganghua Yang [c], Chao Cai [b], Shixuan Chen [a,b,*], Yongjin Fang [e,**], Wenbing Wan [c,***]

[a] Department of Burn and Plastic Surgery, Department of Wound Repair Surgery, Affiliated Hospital of Nantong University, Nantong, Jiangsu, 226001, China
[b] Zhejiang Engineering Research Center for Tissue Repair Materials, Wenzhou Institute, University of Chinese Academy of Sciences, Wenzhou, Zhejiang, 325000, China
[c] Department of Orthopaedic Surgery, Institute of Orthopedics of Jiangxi Province and Jiangxi Provincial Key Laboratory of Spine and Spinal Cord Disease, The Second Affiliated Hospital, Jiangxi Medical College, Nanchang University, Nanchang, Jiangxi, 330006, China
[d] Department of Thyroid Surgery, First Affiliated Hospital of Sun Yat-sen University, Guangzhou, Guangdong, 510080, China
[e] Department of Otolaryngology, Affiliated Jinhua Hospital, Zhejiang University School of Medicine, Jinhua, Zhejiang, 321000, China

ARTICLE INFO

Keywords:
Wound infection
Antibacterial
Photothermal therapy
Wound healing

ABSTRACT

Wound infections are prevalent and can result in prolonged healing times. In this study, we referred to the "trap-capture-kill" antibacterial strategy to create a wound dressing (DS/PDA@GO-L) by coupling graphene oxide (GO) with lysine and coating it onto the decellularized mushroom stem (DS) using polydopamine (PDA). The mechanism of action of the bacteria-killing process involves lysine chemotaxis and the siphoning effect of DS aerogel, with the process of killing the bacteria being initiated via near-infrared photothermal treatment. In vitro studies demonstrated that DS/PDA@GO-L exhibited excellent blood and cell compatibility, while in vivo experiments revealed its remarkable efficacy in combating bacterial infections. Specifically, the combination of DS/PDA@GO-L with photothermal therapy led to the elimination of over 95 % of *S. aureus*, *E. coli*, and *Pseudomonas aeruginosa*. Furthermore, the aerogel, when used in conjunction with photothermal therapy, significantly reduced bacterial infection at the wound site and accelerated wound healing. During the wound's proliferative phase, it notably enhanced vascularization and extracellular matrix deposition. Furthermore, immunohistochemical staining revealed that bacterial clearance led to a reduction in pro-inflammatory responses and a decrease in the expression of pro-inflammatory cytokines, thereby restoring the wound's inflammatory environment to a pro-regenerative state. Taken together, the developed DS/PDA@GO-L holds great potential in the field of infected skin wound healing.

1. Introduction

Infectious wounds pose a significant clinical challenge due to their propensity for delayed healing, persistent inflammation, and the increasing prevalence of antibiotic-resistant pathogens [1,2]. Although antibiotics have been widely used in anti-infection treatment, their overuse and misuse have accelerated the emergence of multidrug-resistant bacteria, necessitating alternative therapeutic approaches [3]. Recent advances in wound healing research have focused on the development of antibiotic-free strategies, leveraging innovative biomaterials with antibacterial properties to address these challenges. To this end, people have developed a variety of antibacterial materials for antibiotic-free treatment, including **antimicrobial peptides** [4,5], cationic polymers [6,7], oxygen free radicals [8,9], etc. Despite the evident benefits of these materials in terms of their excellent antibacterial properties, there are inherent limitations in terms of their practical applications. For instance, cationic polymers require chemical synthesis, which necessitates the use of organic solvents or catalysts, thereby

Peer review under the responsibility of editorial board of Bioactive Materials.
* Corresponding author. Department of Burn and Plastic Surgery, Department of Wound Repair Surgery, Affiliated Hospital of Nantong University, Nantong, Jiangsu, 226001, China.
** Corresponding author.
*** Corresponding author.
E-mail addresses: chensx@ucas.ac.cn (S. Chen), 5fyj@sina.com (Y. Fang), ndefy15220@ncu.edu.cn (W. Wan).
[1] C. Zhang, S. Fan, and J. Zhang contributed equally to this work.

https://doi.org/10.1016/j.bioactmat.2025.03.022
Received 20 January 2025; Received in revised form 22 March 2025; Accepted 26 March 2025

compromising their biocompatibility and resulting in a high hemolysis rate [10]. In light of these advancements, the current focus is on developing next-generation wound care solutions that integrate robust antibacterial efficacy with biocompatibility and regenerative properties. Such strategies are critical for addressing the growing burden of infected wounds in clinical settings and advancing patient outcomes.

When treating infected wounds, the conventional approach typically involves the direct application of antibacterial materials to the wound surface. However, bacteria do not remain confined to the surface of the wound; rather, they frequently invade deeper into the tissue, a particularly problematic occurrence in cases of wound infection caused by biofilms. Biofilm formation creates a protective barrier that not only shields the bacteria but also seals the wound, making it significantly more challenging to eliminate the infection completely. Effective treatment strategies must therefore address both surface-level and deep-tissue bacteria. The chemotactic properties of bacteria themselves provide ideas for our research. One promising avenue involves leveraging the chemotactic properties of bacteria. Bacterial chemotaxis refers to the movement of bacteria toward favorable environments by sensing environmental stimuli, particularly chemical gradients [11]. This mechanism allows bacteria to migrate toward nutrients, such as glucose and amino acids, which are essential for their survival [12]. Xing et al. demonstrated that lysine-loaded nanoparticles can induce bacterial chemotaxis, offering a novel approach to manipulating bacterial behavior for therapeutic purposes [13]. In addition, the lysine biosynthetic pathway, in which lysine is involved, is essential for the bacteria to survive. It inspires a novel approach to addressing bacterial infections in wounds. If bacteria can first be induced to migrate out of the biofilm or deep tissue of the wound through chemotaxis and subsequently eliminated, it could represent a highly effective therapeutic strategy.

After bacteria are effectively "fished" out, the critical next step is to kill the bacteria rapidly and efficiently to prevent further infection and promote wound healing. Several advanced approaches have been developed to address this issue. Among the various antibacterial strategies, photothermal therapy (PTT) has emerged as a promising approach due to its mild yet effective mechanism, high efficiency, spatiotemporal controllability, and deep tissue penetration [14–16]. Unlike traditional antibiotics, PTT leverages near-infrared (NIR) radiation to induce localized hyperthermia, disrupting bacterial membranes and effectively killing pathogens without promoting bacterial resistance. This characteristic makes PTT a compelling alternative to conventional antibacterial treatments, particularly in the context of drug-resistant infections [17]. Recent advancements in photothermal functional materials have expanded the potential of PTT for clinical applications. Inorganic nanomaterials such as noble metal nanoparticles (e.g., gold and copper) [18–20], and carbon-based materials (e.g., carbon nanotubes and graphene derivatives) [21,22], have been extensively explored for their antibacterial properties. Among these, graphene oxide (GO) has gained attention due to its exceptional optical properties, which enable efficient light absorption and conversion into heat [23]. Furthermore, GO exhibits high water solubility and a surface enriched with functional groups like carboxyl and hydroxyl groups, facilitating chemical modification and functionalization [24,25].

In our previous study, we have reported a decellularized *Agaricus bisporus* hemostatic sponge (DS foam) [26]. First of all, DS sponges have been proven to have good cell adhesion and proliferation abilities, blood compatibility, as well as it can be well integrated with surrounding tissues [26]. Moreover, the interior of the DS sponge exhibits a large number of vertically aligned channels. The unique parallel-arranged-channel structure of DS sponge endows it with good liquid absorption ability and capillary action, which is beneficial for absorbing wound exudate [27]. In addition, these vertically aligned can induce cells to migrate from the wound bed to the center of the wound, accelerating wound vascularization and the formation of granulation tissue [28]. According to the aforementioned reports, we hypothesized that using DS sponge as a substrate matrix to design an antibacterial material that could first trap bacteria and then kill them. For one thing, lysine was employed as a modulator for the GO, serving as both a bacterial trap and a photothermal conversion material. For another, the polymerization reaction of dopamine was utilized to anchor lysine-modified GO to the surface of DS sponge. Moreover, in addition to quickly absorbing wound exudate, the interconnected channel structure of the DS sponge can also be used to recruit and store bacteria, facilitating the concentrated elimination of bacteria. In the present study, the effects of functionalized DS foam on bacteria elimination, regulation of local inflammation, and wound healing will be explored.

2. Materials and methods

2.1. Materials

Agaricus bisporus was purchased from China Resources Vanguard Supermarket (Nanchang, China). GO (catalog number G405797), lysine (catalog number 56-87-1), dopamine hydrochloride (catalog number 51-61-6), and Tris-HCl (catalog number 1185-53-1, pH = 8.5) were purchased from Aladdin Biochemical Technology Co., Ltd. (Shanghai, China). N-Hydroxysuccinimide (NHS, catalog number 6066-82-6) and N-(3-dimethylaminopropyl)-N′-ethylcarbodiimide hydrochloride (EDC, catalog number 7084-11-9) were purchased from Sigma-Aldrich (St. Louis, USA). Sodium dodecyl sulfate (SDS, 98 %, AR, catalog number 151-21-3) and sodium chlorite bleach (AR, catalog number 7758-19-2) were provided by Shanghai MacLean Biochemical Technology Co., Ltd. Fetal bovine serum (FBS, catalog number 10099-141C) and Dulbecco's modified Eagle's medium (DMEM, catalog number 11965118) were from Gibco, Invitrogen, USA. Modified Giemsa staining solution (catalog number C0131) was purchased from Beyotime (Shanghai, China). Anti-Ly6G antibody (catalog number 551459) was purchased from BD pharmingen. Anti-CCR7 antibody (catalog number ab253187) was purchased from Abcam (Shanghai, China). Anti-CD206 antibody (catalog number PA5-101657) was purchased from Invitrogen. Anti-IL4 antibody (catalog number TA5142M), anti-IL6 antibody (catalog number TD6084), anti-IL10 antibody (catalog number TD6894) and anti-TNF-α antibody (catalog number TA7014) were all provided by Abmart (Shanghai, China).

2.2. Preparation of GO-L

GO-L was synthesized using an amide reaction according to literature reports [29]. Briefly, 100 mg GO (0.2 % w/v), 0.25 g NHS (0.5 % w/v) and 0.25 g EDC (0.5 % w/v) were successively added to 50 mL of Tris-HCl solution and stirred for 30 min, then 0.3 g Lysine (0.6 % w/v) was added and stirred for 12 h, and finally centrifuged at 8000 g for 10 min, washed 3 times, and freeze-dried to obtain GO-L.

2.3. Preparation of DS/PDA

DS foams (10 × 10 × 3 mm) were obtained from decellularized stems of *Agaricus dispora* according to previous studies [26]. 100 mg DS foam (0.1 % w/v) and 200 mg PDA (0.2 % w/v) were added to 100 mL of Tris-HCl solution. After 24 h of stirring at room temperature, and then the DS/PDA was washed three times. Freeze dried overnight.

2.4. Preparation of DS/PDA@GO-L

DS/PDA@GO-L was produced as previously reported [30]. In brief, 100 mg DS/PDA (0.1 % w/v) and 100 mL Tris-HCl (10 mM, pH 8.5) were added to a beaker, followed by the addition of 80 mg GO-L (0.08 % w/v) and stirring for 12 h at room temperature. Next, DS/PDA@GO-L was collected and washed 3 times. The samples were dried under vacuum overnight.

2.5. Physical characterization

The morphology of GO and GO-L was tested by Transmission Electron Microscopy (TEM) (Tecnai F30, Holland). The particle sizes of GO and GO-L were recorded by Zetasizer Nano ZSP (Malvern, UK). FITR spectra were recorded using Nivolet IS20 (Thermo Scientific, China). The surface morphology of DS/PDA@GO-L was observed using scanning electron microscopy (SEM) (FEI/Phillips XL30 FEG). Elemental composition information of DS/PDA@GO-L was studied by X-ray photoelectron spectroscopy (XPS, Kratos AXIS 165, UK).

2.6. Swelling ratio and porosity measurement

The samples were immersed in PBS solution (pH 7.4, 37 °C) and removed after 24 h. We wiped off the water attached to the surface and weighed the samples. Wb and Wa are the weight of the sample before and after water absorption, respectively, and Ss is the swelling ratio of samples.

$$Swelling\ ratio\ (\%) = (Wa - Wb) / Wb \times 100\%$$

The porosity of DS, DS/PDA and DS/PDA@GO-L groups were measured by liquid displacement method. The initial weight (m1) and volume (V) of the sample were assessed, then we immersed them in absolute ethanol and measured their mass by wiping off the liquid with filter paper until the mass held constant Porosity was calculated as follows: (ρ is the density of alcohol) (n = 3):

$$Porosity\ (\%) = (m2 - m1) / \rho v \times 100\%$$

2.7. Evaluation of antibacterial properties of DS/PDA@GO-L

We evaluated the antibacterial properties of DS/PDA@GO-L using a plate count assay [31]. To evaluate whether DS/PDA@GO-L has spectral antibacterial properties, *Staphylococcus aureus* (*S. aureus*), *Escherichia coli* (*E. coli*) and *Pseudomonas aeruginosa* (*PAO1*) were selected for the experiments. In brief, 50 μL bacterial solution from the plateau phase were added droppers to the sample. The laser irradiation at 808 nm was performed (1 W/cm^2) for 5 and 10 min. The bacteria were then washed down diluted using PBS and spread evenly on nutrient agar plates. After incubation for 24 h at 37 °C, colonies were photographed and counted on nutrient agar plates.

Calcein-AM/PI staining was used to further test the antibacterial properties of the materials by staining the bacteria after different treatments. 100 μL *PAO1* bacterial solution and different samples were mixed and incubated at 37 °C specifically. After laser irradiation (808 nm, 1.0 W/cm^2) or no laser irradiation, bacteria were washed down with 0.9 % NaCl solution, collected by centrifugation (8000 rpm/min, 5min), stained with Calcein-AM and PI (Solarbio, China) for 15 min, and rinsed 3 times with 0.9 % NaCl solution. Finally, the staining was observed by fluorescence microscopy (DM6B, Leica, Germany). We further used scanning electron microscopy (SEM, FEI/Phillips XL30 FEG) to observe the morphology of bacteria after different treatments.

2.8. Biocompatibility evaluation of DS/PDA@GO-L

Red blood cells obtained from whole blood of SD rats were diluted to 5 % with PBS solution. The powdered sample was dissolved in PBS to obtain different solutions (2500 μg/mL, 1250 μg/mL, and 625 μg/mL). Equal volumes of the red blood cell solution and the sample solution were mixed and incubated in an incubator at 37 °C for 1 h. Next, the solution was centrifuged at 1000 rpm for 10 min, and the supernatant was taken to detect the OD value at 562 nm.

Hemolysis rate (%) =(Os-Op)/(Ow-Op) × 100 %, Os, Ow and Op were OD values of samples, water and PBS, respectively (n = 3).

The proliferation of L929 cells was assessed using the CCK-8 assay. 1 × 10^4 L929 cells were seeded into a 96-well plate and cultured overnight. Then, the extract was added to the 96-well plate and continued to be cultured. At the indicated time points, the culture medium was replaced with 100 μL of 10 % CCK-8 solution and then incubated for another 2 h. Subsequently, the absorbance at 450 nm was measured using a microplate reader (BioTek, USA).

The biocompatibility of DS/PDA@GO-L was detected by Live/Dead Cell Staining Kit (Solarbio, China). On days 1 and 3, cells were stained according to the manufacturer's operating manual. The cells were photographed using a fluorescence microscope (DM6B, Leica, Germany). In addition, the cell-loaded DS/PDA@GO-L foams were collected and fixed with 4 % paraformaldehyde, and then the samples were subjected to gradient dehydration and freeze-dried, and the cell morphology was photographed under a scanning electron microscope.

2.9. In vivo wound healing

We evaluated the infected wound healing properties of DS/PDA@GO-L using a *S. aureus* rat infected skin defect model [32]. All animal experiments were approved by the Animal Experiment Ethics Committee of Wenzhou Institute, University of Chinese Academy of Science in Wenzhou, China (WIUCAS24092402).

An infected skin defect model was established on the back of rats after hair removal. The wound diameter was about 10 mm, and the number of *S. aureus* bacteria injected was 10^7 CFU. After 12 h, the wound was treated with DS, DS/PDA, and DS/PDA@GO-L, respectively. The illumination group was irradiated with 808 nm light (1 W/cm^2) for 10 min. At the same time, on the 3rd and 7th days, bacterial exudate from the wound was collected with a wet cotton swab, dissolved in 1 mL of 0.9 % NaCl solution for culture, and the number of bacteria was counted by the standard plate counting method. Wound photos were taken at the specified time points and wound skin tissue samples were collected, fixed with 4 % paraformaldehyde solution, and sliced and stained.

2.10. Giemsa staining

The skin of the infected wound of the rats was taken on the 7th day after different treatment, and was spread at 60 °C for 1 h, then dewaxed in xylene and hydrated in a gradient manner (100 % ethanol 8–10 min, 95 % ethanol 4–6 min, 90 % ethanol 4–6 min, 80 % ethanol 4–6 min, 70 % ethanol 5 min, pure water 5 min). Dilute the Giemsa staining solution 20 times, take 500 μL of the diluted staining solution and drop it on the tissue section, observe under the microscope and color for 20 s. Place the section in a fume hood, air dry and seal the section, scan to obtain the picture, and observe the *S. aureus* colony on the rat wound surface.

2.11. Immunohistochemical staining

Following a week-long treatment period, skin tissues from infected wounds of rats were collected and fixed with 4 % paraformaldehyde. Subsequently, the tissue samples were dehydrated, embedded, sectioned and stained for immunohistochemistry. Sections were first subjected to pretreatment steps such as antigen repair, removal of endogenous peroxidase and sealing. During the staining process, PBS was used to dilute primary antibodies at the following ratios: Ly6G (1/600), CCR7 (1/200), CD206 (1/200), IL-6 (1/300), TNF-α (1/300), IL-4 (1/300), and IL-10 (1/300). Sections were then incubated overnight at room temperature, washed, and secondary antibodies were used. The DAB colour development reaction time was 20–30 s, followed by hematoxylin staining for 1 min. Finally, the inflammatory response of rat wounds was assessed by rinsing under running water for 5 min, hydrochloric acid fractionation for 3 s, dehydration, xylene permeabilisation and sealing.

2.12. Histological observations

After 3 and 7 days of treatment, the infected wounds and

surrounding skin of rats were fixed with 4 % paraformaldehyde and then stained with hematoxylin-eosin (H&E). The skin tissue was first dehydrated, embedded, and sliced, then dewaxed and hydrated. After hematoxylin staining, the wounds were rinsed with tap water, differentiated with 0.5 % hydrochloric acid alcohol, and blued with tap water. The formation of granulation tissue and re-epithelialization of the infected wounds of rats were evaluated by eosin staining. Masson trichrome staining was then performed to evaluate the collagen deposition and vascular regeneration of the wounds of rats after 7 days of treatment.

2.13. Statistical analysis

Data were analyzed using Graphpad or Origin software. Data are presented as mean ± standard deviation (SD). One-way analysis of variance (ANOVA) was performed to determine statistically significant

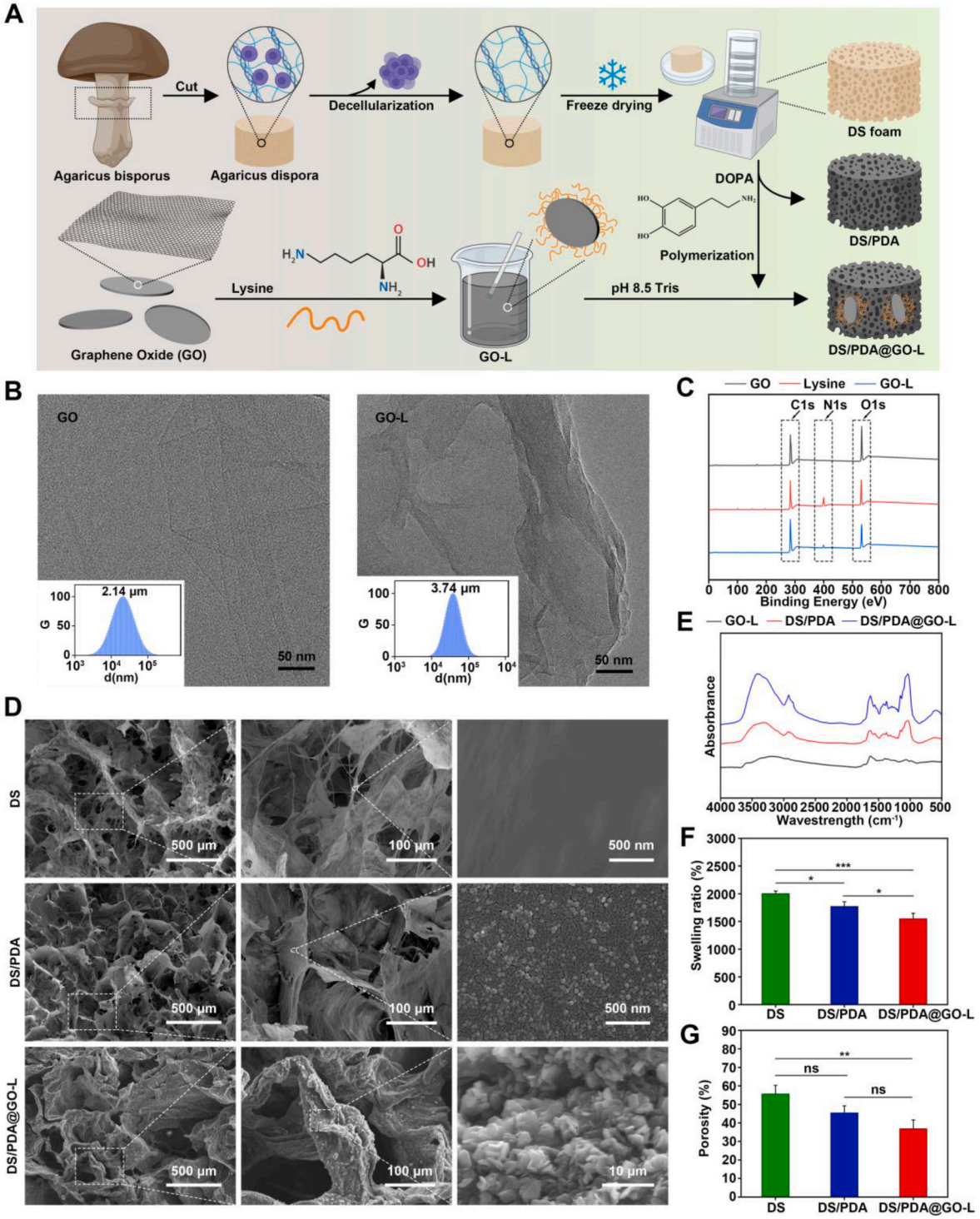

Fig. 1. Fabrication and characterization of GO-L and DS/PDA@GO-L. (A) Schematic diagram of the preparation of DS, DS/PDA, and DS/PDA@GO-L. (B) TEM images and particle size distribution of GO and GO-L. (C) XPS spectra of GO, lysine, and GO-L. (D) SEM images of DS, DS/PDA, and DS/PDA@GO-L. (E) FTIR spectra of DS, DS/PDA, and DS/PDA@GO-L. Swelling ratio (F) and porosity (G) of DS, DS/PDA, and DS/PDA@GO-L.

differences (*p < 0.05, **p < 0.01, ***p < 0.001, and ****p < 0.0001).

3. Results

3.1. The preparation and characterization of DS/PDA@GO-L

Fig. 1A illustrates the preparation process of DS/PDA@GO-L. Decellularized *Agaricus bisporus* was combined with lysine-modified graphene oxide (GO-L) through dopamine self-polymerization at pH 8.5. Fig. 1B shows that synthesized GO exhibited a flaky, naturally unfolding structure, while lysine grafting resulted in a rougher surface, increased thickness, and irregular curling. Particle size analysis revealed larger dimensions for GO-L (3.74 μm) compared to GO (2.14 μm), likely due to lysine aggregation during synthesis. XPS analysis confirmed lysine grafting on GO (Fig. 1C), validating the successful synthesis of GO-L. The macroscopic images of DS, DS/PDA, and DS/PDA@GO-L show their porous structures (Fig. S1). The DS sponge showed larger pores in the SEM image (Fig. 1D), which slightly decreased after coating with PDA due to uniform deposition. In DS/PDA@GO-L, pore size decreased significantly, with surface sediment accumulation indicating successful composite formation. Fourier transform infrared (FTIR) analysis (Fig. 1E) identified characteristic absorption peaks at 2922 and 1035 cm^{-1} [33], corroborating the successful integration of GO-L with DS/PDA. These characteristics facilitate wound exudate absorption. XPS further confirmed nitrogen presence in GO-L-modified DS (Fig. S2). Porosity and swelling ratio measurements showed decreases in DS/PDA and DS/PDA@GO-L due to pore filling by PDA and GO-L. However, DS/PDA@GO-L retained a swelling rate of 1549.96 ± 97.43 % and a porosity of 36.89 ± 4.68 % (Fig. 1F and G), ensuring adequate water absorption and porosity for infected wound management. These characteristics facilitate wound exudate absorption, keep wounds dry, and support cellular proliferation and nutrient exchange [34].

3.2. Photothermal properties of DS/PDA@GO-L

As shown in Fig. 2A, the DS does not have a photothermal effect, while the adsorption of PDA makes DS (DS/PDA) possess a photothermal effect. By compression, DS/PDA@GO-L exhibited superior photothermal performance, primarily due to the large specific surface area and high thermal conductivity of GO. This enhanced photothermal property supports effective antibacterial photothermal therapy (PTT) and facilitates the reconstruction of the infected wound microenvironment [35]. Thermal imaging results revealed that under near-infrared (NIR) irradiation (1 W/cm^2), the temperature of DS/PDA@GO-L increased from 23.2 °C to 51.4 °C within 10 min, outperforming DS (22.9 °C–25.1 °C) and DS/PDA (23.4 °C–45.7 °C). Fig. 2B–D further confirms DS/PDA@GO-L's rapid and efficient NIR-induced heat generation, underscoring its ability to effectively convert NIR light into thermal energy. The enhanced photothermal conversion efficiency of DS/PDA@GO-L, compared to DS and DS/PDA, is likely attributed to the addition of PDA and GO [36]. Photostability testing demonstrated that DS/PDA@GO-L retained stable thermal performance across five cycles of NIR laser irradiation (1 W/cm^2, 808 nm) (Fig. 2E). In order to further verify the photothermal effect of the DS/PDA@GO-L in vivo, we implanted the DS/PDA@GO-L underneath the skin of the head. Under 808 nm laser irradiation for 10 min, the temperature of local area treated with DS/PDA@GO-L reached 46.3 °C, which was higher than the 41.5 °C observed for DS/PDA (Fig. 2F and G). These findings confirm DS/PDA@GO-L's robust photothermal performance and stability, making it a promising material for PTT-based antibacterial applications (Fig. 2H). Eliminating bacterial infection in the wound is conducive to changing the inflammatory microenvironment of the wound from a pro-inflammatory type to a pro-regenerative type, thereby further accelerating wound closure (Fig. 2I).

3.3. In vitro biocompatibility evaluation of DS/PDA@GO-L

Following, we examined the biocompatibility of the developed DS/PDA@GO-L. Firstly, we explored the blood compatibility of DS/PDA@GO-L (Fig. 3A). Hemolysis testing was performed using erythrocytes, with ultra-pure water and PBS serving as positive and negative controls, respectively. At the highest concentration (2.5 mg/mL), the hemolysis rate of DS/PDA@GO-L was only 3.64 ± 0.63 %, well below the international safety threshold of 5 %. Hemolysis rates were 0.93 ± 0.32 % (0.625 mg/mL), 1.99 ± 0.20 % (1.25 mg/mL), and 3.64 ± 0.63 % (2.5 mg/mL), indicating excellent hemocompatibility suitable for therapeutic use (Fig. 3B and C). Then, we continued to examine the cytocompatibility of the DS/PDA@GO-L (Fig. 3D). The L929 fibroblasts were cultured with extracts (0.2 g/mL) of DS, DS/PDA, and DS/PDA@GO-L sponges for 1, 3, and 5 days. As shown in Fig. 3E, no significant differences in cell viability were observed between the treatment and control groups, confirming minimal cytotoxicity. The Live/Dead staining revealed abundant viable cells (green) and only a few dead cells (red) were found (Fig. 3F). SEM imaging demonstrated that L929 fibroblasts treated with DS/PDA or DS/PDA@GO-L spread well, showing no notable morphological changes or growth inhibition (Fig. 3G). These findings establish the excellent biocompatibility of DS/PDA@GO-L for wound management.

3.4. In vitro antibacterial test of DS/PDA@GO-L under NIR irradiation

To verify our scaffold's "Trap and Capture" ability. We immersed the scaffold material in a low-concentration bacterial solution and cultured it for 30 min, then placed it in a Petri dish and continued to culture it for 24 h. SEM characterization showed that the surface, interior, and bottom surfaces of the materials in the DS/PDA@GO-L group could attract more bacteria (Fig. S3), which was caused by the chemotaxis of lysine.

To evaluate bactericidal efficacy, gram-positive *Staphylococcus aureus* (*S. aureus*), gram-negative *Escherichia coli* (*E. coli*), and *Pseudomonas aeruginosa* (*PAO1*) were tested. The bacteria treated with DS or without treatment as the control because DS has no photothermal effects. Each bacterial solution (100 μL) was introduced onto the DS/PDA and DS/PDA@GO-L sponges and irradiated with near-infrared (NIR) light (Fig. 4A). Plate count analysis revealed significant antibacterial effects in the DS/PDA and DS/PDA@GO-L groups in combination with NIR exposure compared to control, DS, DS/PDA only, and DS/PDA@GO-L only groups. In addition, prolonging the NIR radiation time (10 min) is more conducive to killing bacteria than 5 min NIR radiation. Moreover, the DS/PDA@GO-L + NIR group showed a more pronounced antibacterial effect than DS/PDA + NIR, likely due to the higher temperature achieved during NIR irradiation. Specifically, the DS/PDA@GO-L + NIR group exhibited >95 % antibacterial efficacy against all three bacterial strains, confirming its broad-spectrum antibacterial activity (Fig. 4B–4D). The antibacterial effect was further assessed using Live/Dead assay (Fig. 4E). Without NIR, bacteria predominantly survived (green fluorescence) in the control, DS, DS/PDA only, and DS/PDA@GO-L only groups. While NIR irradiation led to significant bacterial death (red fluorescence) in both DS/PDA and DS/PDA@GO-L groups, with DS/PDA@GO-L showing more extensive bacterial killing, consistent with plate count results. Morphological changes in bacteria were observed via SEM after a 12-h co-culture (Fig. 4F). Without NIR exposure, *S. aureus* retained a spherical shape, *E. coli* had a rod-like morphology, and *PAO1* had a smooth rod structure. After NIR irradiation, all bacteria cultured on the DS/PDA and DS/PDA@GO-L exhibited shrinkage, desiccation, and rupture morphologies. Moreover, the bacterial cell wall of DS/PDA@GO-L + NIR group collapsed more seriously than DS/PDA + NIR group. These results suggest that DS/PDA@GO-L effectively kills bacteria through a combination of photothermal effects and disruption of bacterial membranes, resulting in bacterial death and structural collapse.

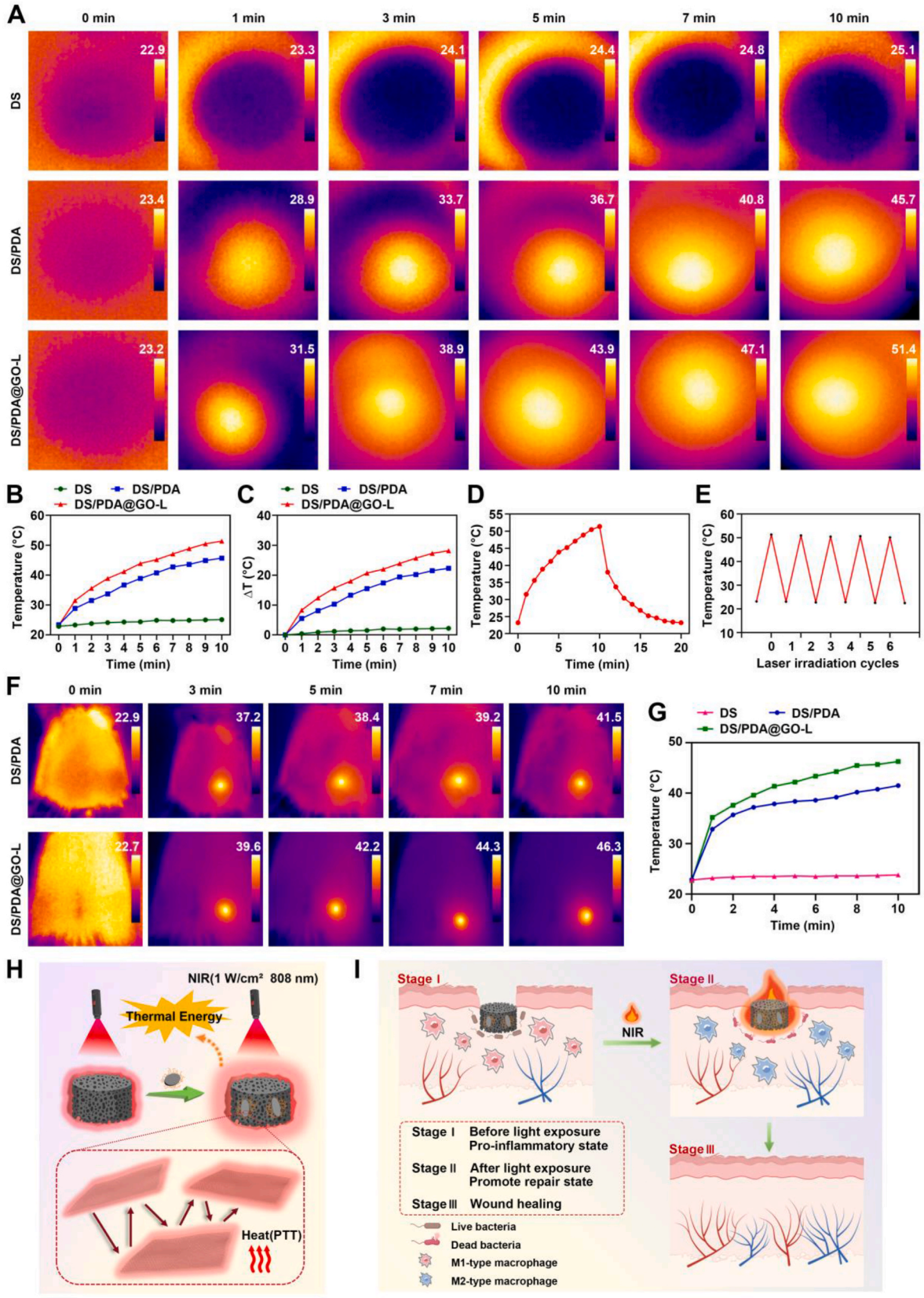

Fig. 2. Photothermal effects of DS/PDA@GO-L in vitro and in vivo. (A) Infrared thermal imaging of DS, DS/PDA, and DS/PDA@GO-L under 808 nm (1 W/cm^2) irradiation. (B) Temperature curves of DS, DS/PDA, and DS/PDA@GO-L irradiated at 808 nm (1 W/cm^2) for 10 min. (C) Temperature increase of DS, DS/PDA, and DS/PDA@GO-L irradiated at 808 nm (1 W/cm^2) for 10 min. (D) Temperature increase and decrease curves of DS/PDA@GO-L irradiated at 808 nm (1 W/cm^2) for 10 min. (E) Heating curve of DS/PDA@GO-L under 808 nm (1 W/cm^2) irradiation with five on/off cycles for 10 min. (F) Thermal imaging of DS/PDA and DS/PDA@GO-L in rats under 808 nm laser irradiation. (G) Temperature change curve during in vivo treatment. (H) Schematic diagram illustrating that the addition of GO enhances the photothermal properties of DS/PDA. (I) Schematic diagram illustrating that photothermal antibacterial can correct abnormal inflammation.

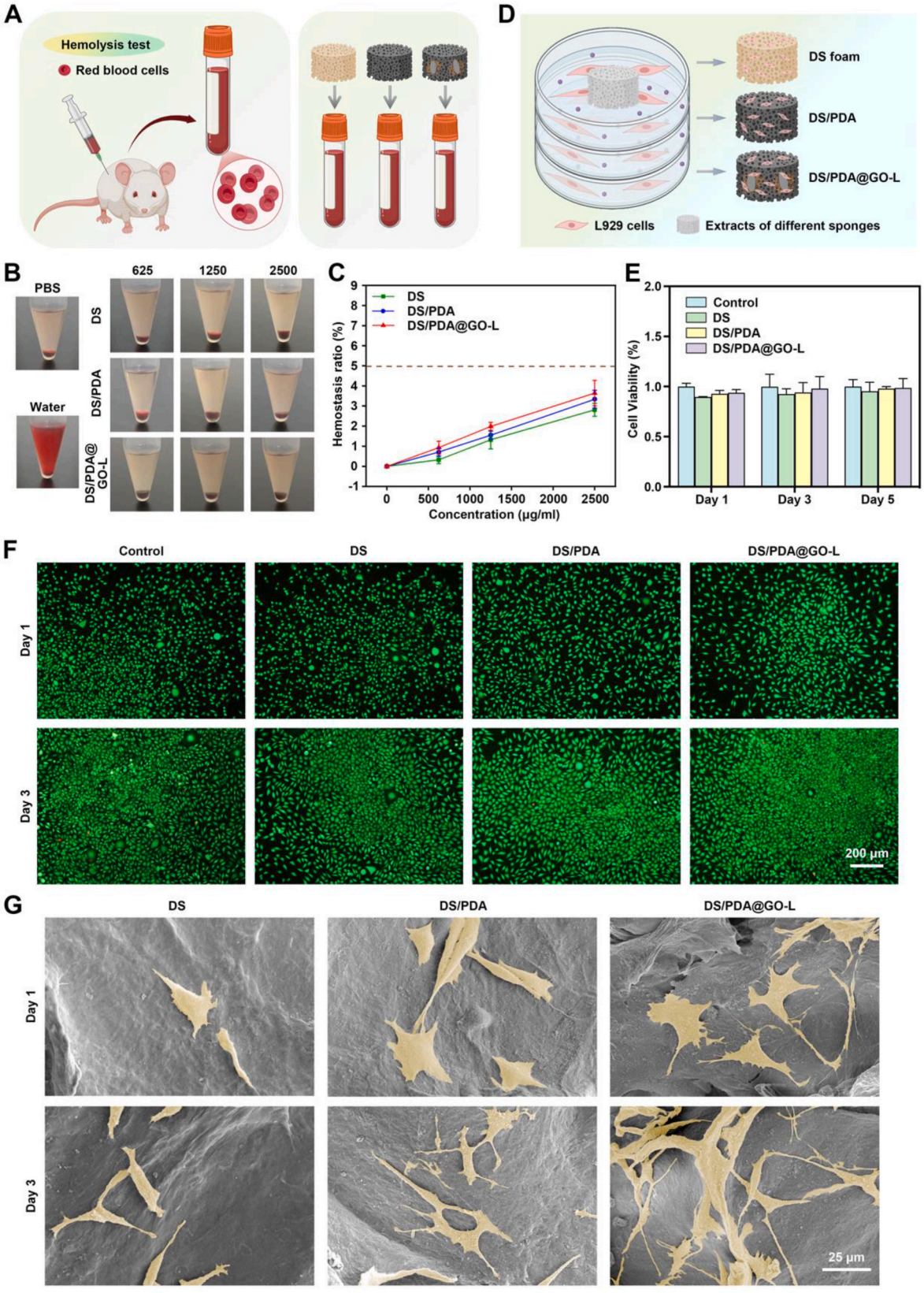

Fig. 3. In vitro biocompatibility of DS/PDA@GO-L. (A) Schematic diagram of blood compatibility experiment. (B) Photograph of hemolytic activity of rat blood. (C) Hemostasis rate incubated with different concentrations of DS, DS/PDA, and DS/PDA@GO-L. (D) Schematic diagram of indirect culture experiment. (E) Cell viability of L929 cells co-cultured with Control, DS, DS/PDA, and DS/PDA@GO-L samples at 405 nm on days 1, 3, and 5. (F) LIVE/DEAD staining of L929 cells co-cultured with Control, DS, DS/PDA and DS/PDA@GO-L samples on days 1 and 3. (Scale bar = 200 μm) (G) SEM images of L929 cells co-cultured with DS, DS/PDA and DS/PDA@GO-L samples on days 1 and 3. Pseudo-color images show the morphology of L929 cells. (Scale bar = 25 μm).

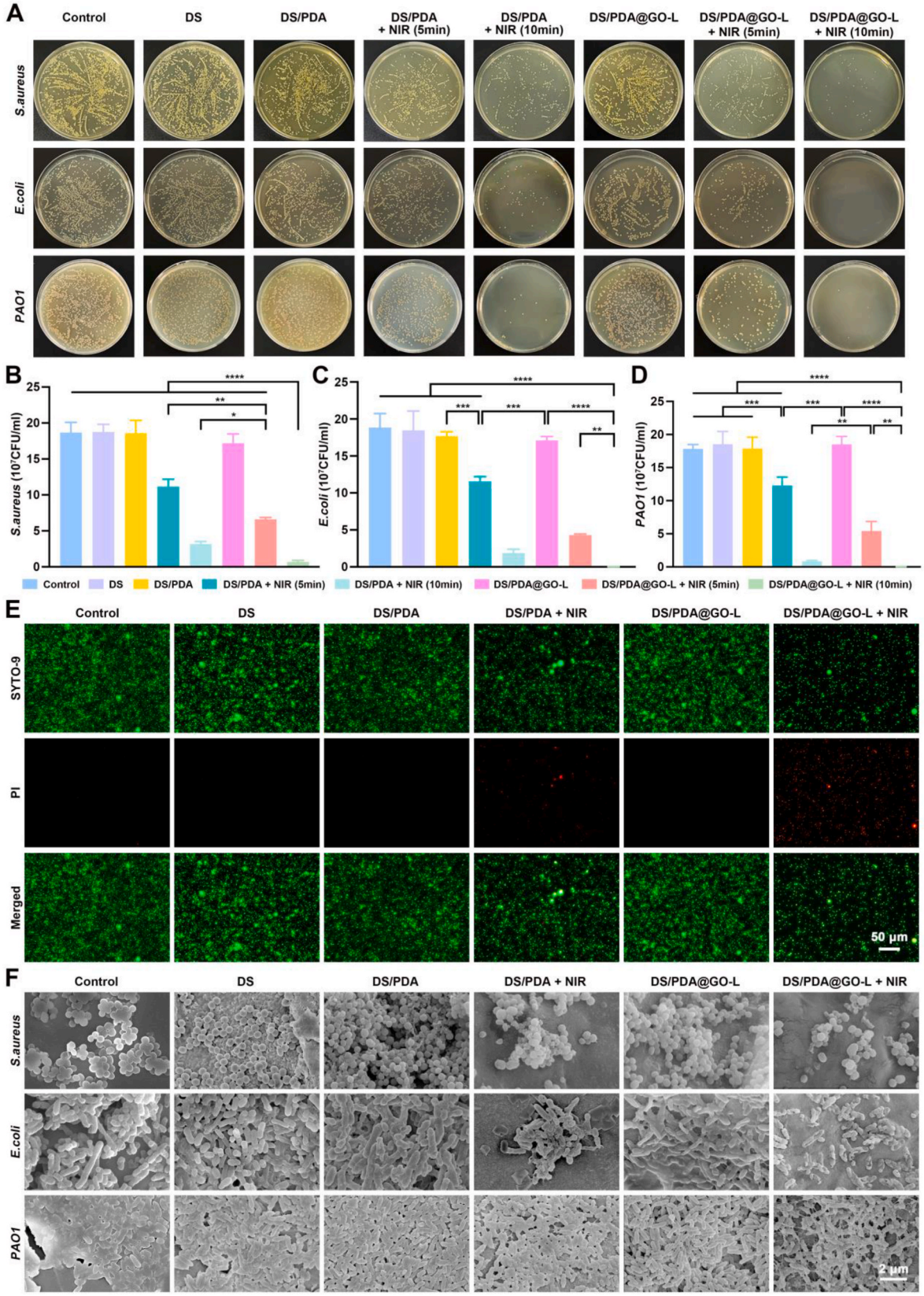

Fig. 4. In vitro antimicrobial capacity of DS/PDA@GO-L under NIR irradiation. (A) Photographs of plate clones of *S. aureus*, *E. coli,* and *PAO1* in different treatment groups. Quantification of colony numbers of *S. aureus* (B), *E. coli* (C) and *PAO1* (D) in different treatment groups. (E) Live and dead staining of *PAO1* bacteria in different treatment groups, the green fluorescence indicates live bacteria and red fluorescence indicates dead bacteria. (Scale bar = 50 μm) (F) SEM images of *S. aureus*, *E. coli* and *PAO1* in different treatment groups. (Scale bar = 2 μm) (****$p < 0.0001$, ***$p < 0.001$, **$p < 0.01$, *$p < 0.05$).

3.5. In vivo antibacterial effect of DS/PDA@GO-L under NIR irradiation

The biodegradation behaviors of the decellularized mushroom scaffold had been investigated in our previous study [26]. We found the decellularized mushroom has a long degradation time in vivo. However, the biocompatibility of the scaffold is very high. After subcutaneous implantation, no obvious fibrous capsule is formed. Cells can infiltrate into the interior of the scaffold and form new granulation tissue. In the presented study, this scaffold was used as a wound dressing. The impact of DS/PDA@GO-L on wound healing was evaluated using an infected wound model, with the healing process recorded (Fig. 5A). In the Control and DS groups, a significant amount of yellow purulent fluid was observed in the wounds (Fig. 5B). In contrast, wounds in the DS/PDA + NIR and DS/PDA@GO-L + NIR groups didn't observe yellow purulent fluid and showed progressive closure. By day 14, the wound healing areas for the Control, DS, DS/PDA, and DS/PDA@GO-L groups were (81.38 ± 0.55)%, (82.77 ± 2.59)%, (83.16 ± 2.93)%, and (85.17 ± 1.72 %), respectively—markedly lower than the DS/PDA + NIR (87.27 ± 1.30)% and DS/PDA@GO-L + NIR group (91.12 ± 0.89)% (Fig. 5C and D). The residual bacteria in wound tissue was assessed using standard plate counting on day 3 and 7 (Fig. 5E and F). The DS/PDA + NIR and DS/PDA@GO-L + NIR groups showed significantly lower bacterial counts compared to all other groups, and the DS/PDA@GO-L + NIR group had less residual bacterial than DS/PDA + NIR group on both day 3 and day 7. The antibacterial rate of the DS/PDA@GO-L + NIR group and DS/PDA + NIR group was (92.94 ± 2.03)% on day 3 and (96.77 ± 3.17)% on day 7. Furthermore, Giemsa staining on day 7 (Fig. 5G) revealed minimal bacteria in the DS/PDA@GO-L + NIR group, while the other groups retained substantial bacterial presence. Quantitatively, the number of *S. aureus* in the DS/PDA@GO-L + NIR group was reduced to only 17.00 ± 3.58 % (Fig. 5H). These in vivo results confirm that DS/PDA@GO-L + NIR significantly reduces bacterial load and promotes wound healing, demonstrating its potent antibacterial and regenerative capabilities.

3.6. Modulation effect of DS/PDA@GO-L on inflammation in vivo under NIR irradiation

To assess the anti-inflammatory effects of DS/PDA@GO-L, the inflammation levels in infected wound tissue were analyzed on day 7, when the inflammatory response is most active. Immunohistochemical staining of monocytes, neutrophils, and macrophages was performed to identify the local inflammation. The DS/PD + NIR and DS/PDA@GO-L + NIR groups demonstrated a significant reduction in the expression of Ly6G (a marker for granulocytes, monocytes, and neutrophils) and CCR7 (indicative of pro-inflammatory M1 macrophages) compared to other groups (Fig. 6A–D). Concurrently, the expression of CD206, a marker for anti-inflammatory M2 macrophages, was notably increased in the DS/PDA + NIR and DS/PDA@GO-L + NIR groups (Fig. 6E and F). Moreover, the ratio between the numbers of M1-type macrophages and the numbers of M2-type macrophages in the DS/PDA + NIR and DS/PDA@GO-L + NIR groups was significantly less than 1, indicating a transition of local inflammation from a pro-inflammatory to a pro-regenerative status (Fig. 6G). Further analysis of inflammatory mediators showed that the DS/PDA + NIR and DS/PDA@GO-L + NIR groups had significantly lower levels of pro-inflammatory cytokines IL-6 and TNF-α in the wound area compared to the other groups (Fig. 7A–D). Conversely, anti-inflammatory cytokines IL-4 and IL-10 were markedly elevated (Fig. 7E–H). These findings indicate after effectively removing bacterial biofilms with DS/PDA + NIR and DS/PDA@GO-L + NIR treatments; these treatments can transform the pro-inflammatory inflammatory response caused by bacterial infection into a normal pro-repairing status, thereby creating a conducive microenvironment for wound healing (Fig. 7I).

3.7. Evaluation of the effect of DS/PDA@GO-L + NIR in promoting the repair of infected wounds

To further evaluate wound healing, H&E staining was performed to assess re-epithelialization and granulation tissue formation. As shown in Fig. 8A, the DS/PDA + NIR and DS/PDA@GO-L + NIR groups exhibited a notably longer epithelial tongue and granulation tissue formation compared to the Control, DS, DS/PDA, and DS/PDA@GO-L groups. Quantitative analysis revealed that on day 7, the thickness of new granulation tissue (Fig. 8B) and the re-epithelialization rate (Fig. 8C) in the DS/PDA + NIR and DS/PDA@GO-L + NIR groups were significantly higher than in the other groups, especially in the DS/PDA@GO-L + NIR group. The granulation tissue thickness was 1.71 ± 0.11 mm, and the re-epithelialization rate reached 72.80 ± 3.61 %, significantly outperforming the other groups. Additionally, Masson staining results (Fig. 8D) indicated more extensive collagen deposition in the DS/PDA@GO-L + NIR group by day 7, with a collagen volume proportion of 82.83 ± 4.26 % (Fig. 8E), far exceeding that of the other groups. Furthermore, vascular density analysis (Fig. 8F) showed that the DS/PDA@GO-L + NIR group had the highest vascular density, at 113.19 ± 5.16/mm^2, indicating enhanced angiogenesis. In conclusion, DS/PDA@GO-L + NIR accelerates wound repair by mitigating inflammation, enhancing collagen deposition, and promoting angiogenesis (Fig. 8G). This demonstrates its potential as a promising therapeutic material for infected wound healing.

4. Discussion

In the presented study, we developed a functionalized decellularized-sponge (DS sponge) according to the principle of Trap-Capture-Kill (TCK) antibacterial system. The lysine and vertically arranged long channels in the scaffold can induce bacteria to migrate from the wound area into the scaffold. After the cell trapping is completed, the trapped bacteria are killed through the photothermal effect of GO in the scaffold. The Trap-Capture-Kill antibacterial system is an innovative approach that integrates the physical, chemical, and biological mechanisms of antibacterial activity. This system offers significant advantages for addressing bacterial infections, particularly in scenarios where traditional antibiotics face limitations, such as the rise of antibiotic resistance [37]. For example, the TCK system can enhance antibacterial efficiency. The synergistic effect of trapping, capturing, and killing ensures that bacteria are not only removed but also effectively eradicated. This multi-step approach minimizes the risk of bacterial escape and regrowth [38]. And it reduces risk of resistance development, the mechanical trapping and physical destruction bypass the reliance on antibiotics. In addition, it has broad-spectrum activity. The TCK system is effective against a wide range of pathogens, including bacteria, fungi, and viruses [39]. This makes it suitable for diverse applications, such as wound dressings. Finally, it also has high biocompatibility and safety. Many TCK systems use biocompatible materials, such as chitosan, hydrogels, or biodegradable polymers, ensuring safety for human cells while targeting pathogens [40].

The "trap" of the presented DS sponge TCK system utilizing bacterial chemotaxis to lysine [41], which is one of nutrients that bacteria love and play an important role in bacteria chemotactic migration [42]. In our study, we just want to use the chemotaxis of bacteria to lysine to "fish" the bacteria out of the wound tissue. On the one hand, it can reduce the difficulty of treating infectious wounds, and on the other hand, it can also improve the inflammatory microenvironment of the wound. The "capture" of the presented DS sponge TCK system depending on large pore size and long channel structure of DS sponge to physically capture bacteria. These structures often mimic natural antimicrobial surfaces like cicada wings or gecko skin, utilizing topographies that attract and immobilize bacteria [43,44]. The porous and parallel long channel structure of DS sponge can store large amounts of migrated bacteria. The "kill" the presented DS sponge TCK system using

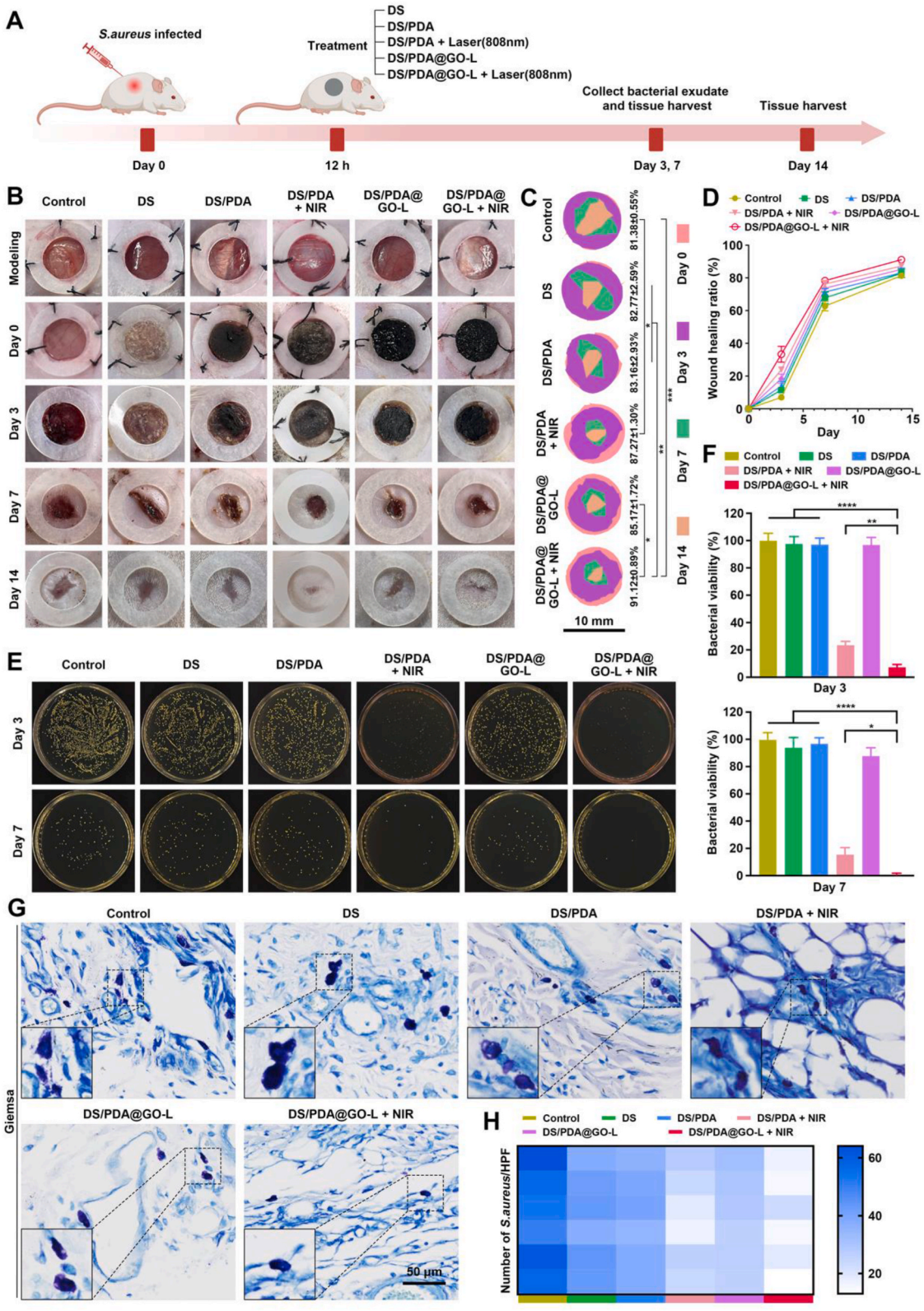

Fig. 5. In vivo wound healing effect of DS/PDA@GO-L under NIR irradiation. (A) Schematic diagram of infected wound construction and treatment. (B) Photos of infected wounds after treatment in the control group, DS group, DS/PDA group, DS/PDA + NIR group, DS/PDA@GO-L group, and DS/PDA@GO-L + NIR group. (C) Schematic diagram of wound closure in vivo in different treatment groups. (D) Wound healing rate in different treatment groups. (E) *S. aureus* colonies in tissue culture of infected wounds on days 3 and 7. (F) Quantification of *S. aureus* colonies in tissue culture of infected wounds on days 3 and 7. (G) Giemsa staining of wound areas in the control group, DS group, DS/PDA group, DS/PDA + NIR group, DS/PDA@GO-L group, and DS/PDA@GO-L + NIR group after 7 days of treatment. (Scale bar = 50 μm) (H) After 7 days of treatment, the detection of *S. aureus* in the wound area of the control group, DS group, DS/PDA group, DS/PDA + NIR group, DS/PDA@GO-L group, and DS/PDA@GO-L + NIR group was quantified. (****$p < 0.0001$, **$p < 0.01$, *$p < 0.05$).

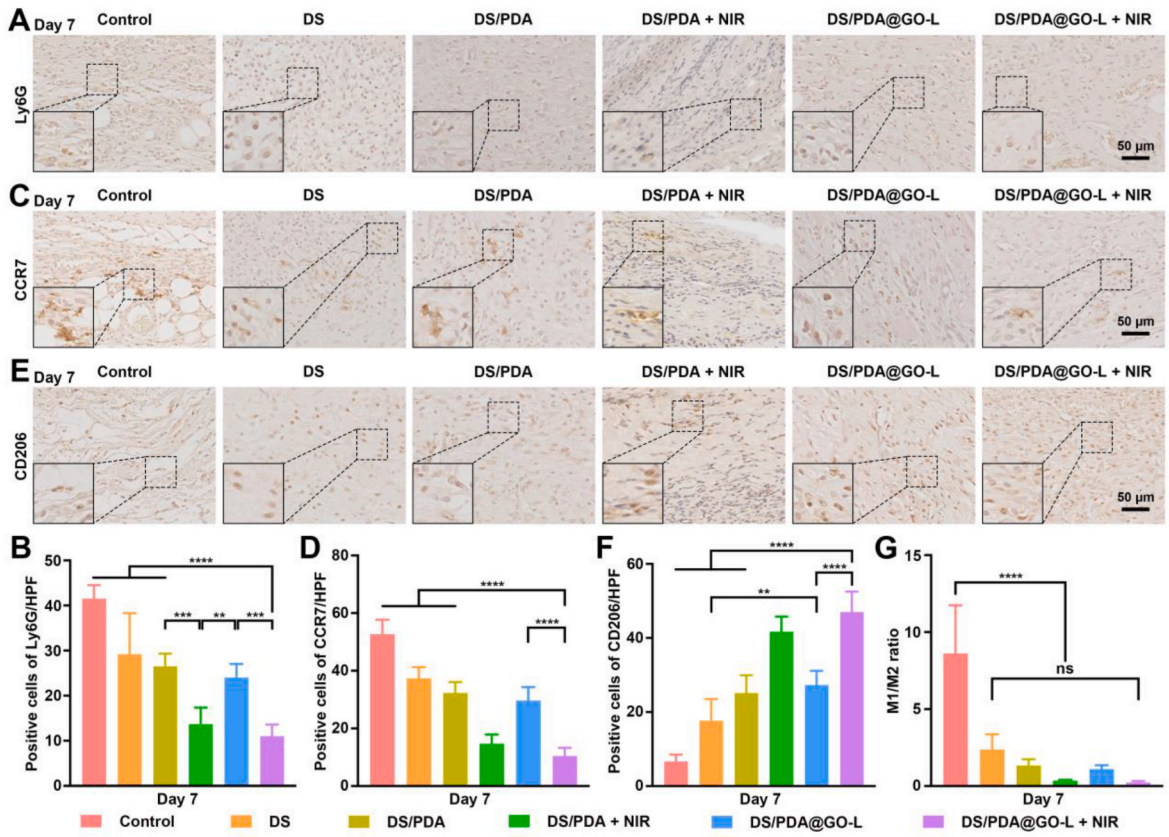

Fig. 6. The assessment of inflammatory responses in infected wound site. (A, B) Expression of Ly6G (a marker for granulocytes, monocytes, and neutrophils) in the central area of the wound in the Control, DS, DS/PDA, DS/PDA + NIR, DS/PDA@GO-L, and DS/PDA@GO-L + NIR groups 7 days after treatment. (C, D) Expression of CCR7 (a marker for pro-inflammatory M1 macrophages) in the central area of the wound in the Control, DS, DS/PDA, DS/PDA + NIR, DS/PDA@GO-L, and DS/PDA@GO-L + NIR groups 7 days after treatment. (E, F) Expression of CD206 (a marker for anti-inflammatory M2 macrophages) in the central area of the wound in the Control, DS, DS/PDA, DS/PDA + NIR, DS/PDA@GO-L, and DS/PDA@GO-L + NIR groups 7 days after treatment. (G) The ratio of the number of M1 macrophages to the number of M2 macrophages in the control group, DS group, DS/PDA group, DS/PDA + NIR group, DS/PDA@GO-L group, and DS/PDA@GO-L + NIR group on day 7. (Scale bar = 50 μm) (****$p < 0.0001$, ***$p < 0.001$, **$p < 0.01$, and ns: not significant).

GO to generate localized heat under light exposure to kill bacteria. Notably, the material demonstrated over 95 % antibacterial activity against both gram-positive and gram-negative pathogens, including *S. aureus*, *E. coli*, and *Pseudomonas aeruginosa*. This synergistic mechanism of bacterial capture and eradication reduces the risk of bacterial escape and regrowth, addressing a critical challenge in managing biofilm-associated infections.

The material's therapeutic effects extend beyond antibacterial activity, as evidenced by its capacity to modulate the wound microenvironment. The DS/PDA@GO-L dressing significantly reduced inflammation by lowering the expression of pro-inflammatory cytokines (IL-6 and TNF-α) while enhancing anti-inflammatory cytokines (IL-4 and IL-10). This shift from a pro-inflammatory to a pro-regenerative state is further supported by the increased polarization of macrophages from the M1 to the M2 phenotype. Such immunomodulatory effects are critical for resolving chronic inflammation and enabling wound repair. In vivo results on a rat model further confirmed the efficacy of the DS/PDA@GO-L system in promoting wound healing. The dressing enhanced vascularization, extracellular matrix deposition, and collagen synthesis, leading to faster wound closure compared to conventional treatments. The thermal stability and biocompatibility of the material ensure safe application, with hemolysis rates well below the international safety threshold and no observed cytotoxic effects.

5. Conclusion

In this study, GO-L particles with bacterial trapping, photothermal enhancement and synergistic antimicrobial effects, inspired by bacterial chemotaxis, were synthesized and loaded onto DS sponge carriers. The particles were then combined using auto-polymerization of dopamine to develop a novel dressing for the treatment of infected skin wounds. The combination of the strong water absorption of the DS tubes and the bacterial chemotaxis of GO-L enhanced the bacterial retention capacity of DS/PDA@GO-L. In addition, DS/PDA@GO-L has excellent biocompatibility, strong antimicrobial effect, and effective anti-inflammatory action, and thus has great potential for clinical translation. Specifically, this dressing is expected to address a key challenge in the management of diabetic ulcers, where the hyperglycaemic microenvironment exacerbates persistent ulcer infection and delays healing. In turn, the dressing has the ability to absorb exudates and disrupt biofilms, making it also suitable for severe burns, with dual functions of infection control and tissue regeneration. Furthermore, the material's capacity to eradicate multidrug-resistant pathogens renders it a promising solution for the prevention of postoperative infections, particularly in high-risk surgical contexts. Subsequent research endeavours will centre on the optimisation of scalability and the validation of its safety.

CRediT authorship contribution statement

Chuwei Zhang: Methodology, Investigation, Formal analysis. **Shuai Fan:** Investigation, Formal analysis. **Jing Zhang:** Methodology, Investigation. **Ganghua Yang:** Formal analysis, Data curation. **Chao Cai:** Writing – original draft, Supervision, Resources. **Shixuan Chen:** Writing

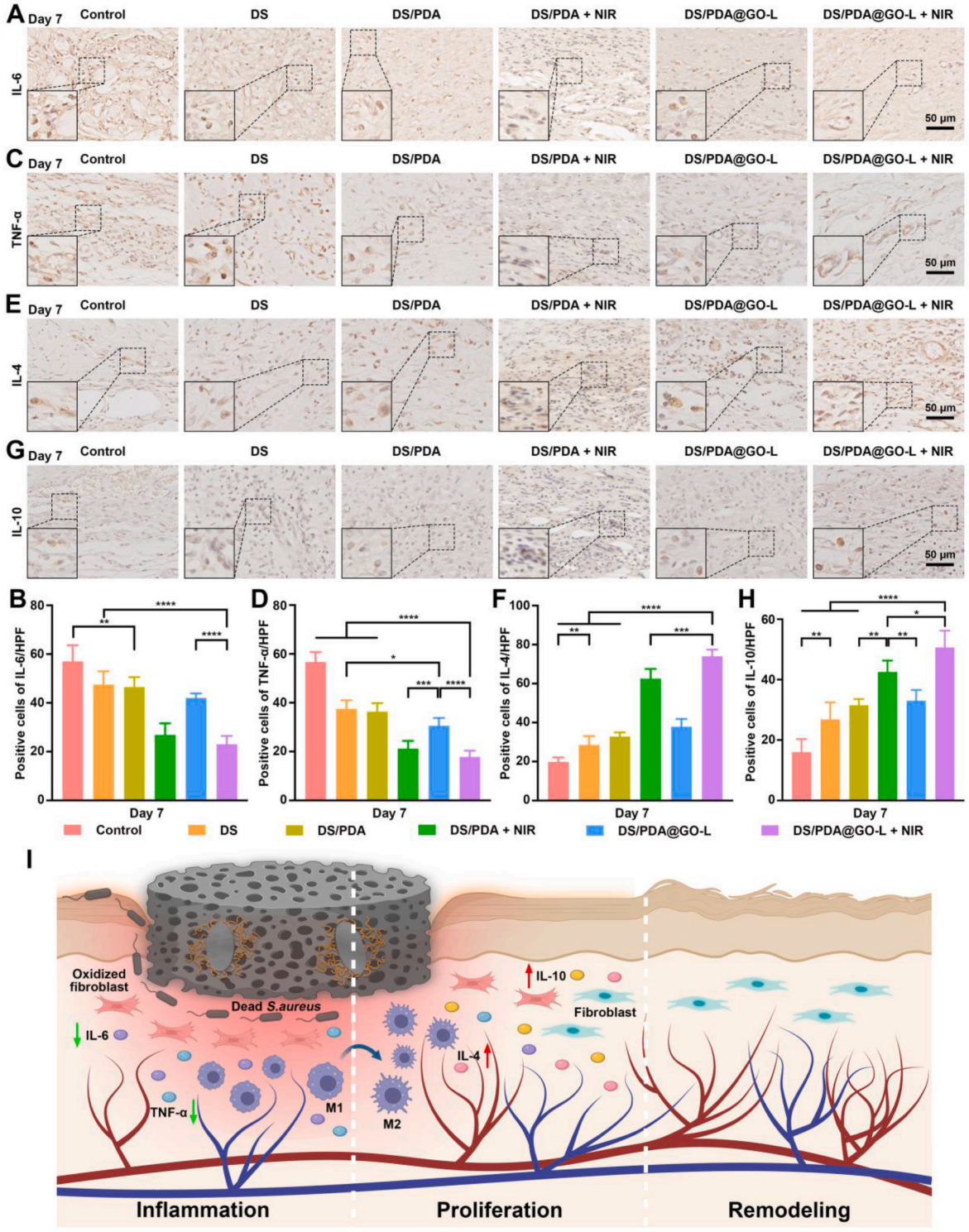

Fig. 7. Characterization of inflammatory and anti-inflammatory factors during early infected wound healing. (A, B) Expression of IL-6 in the central area of the infected wound in the Control, DS, DS/PDA, DS/PDA + NIR, DS/PDA@GO-L, and DS/PDA@GO-L + NIR groups after 7 days of treatment. (C, D) Expression of TNF-α in the central area of the infected wound in the Control, DS, DS/PDA, DS/PDA + NIR, DS/PDA@GO-L, and DS/PDA@GO-L + NIR groups after 7 days of treatment. (E, F) Expression of IL-4 in the central area of the infected wound in the Control, DS, DS/PDA, DS/PDA + NIR, DS/PDA@GO-L, and DS/PDA@GO-L + NIR groups after 7 days of treatment. (G, H) IL-10 expression in the central area of the infected wounds in the control group, DS group, DS/PDA group, DS/PDA + NIR group, DS/PDA@GO-L group, and DS/PDA@GO-L + NIR group after 7 days of treatment. (I) Schematic diagram showing that the inflammatory response returned to normal levels after wound bacteria were cleared. (Scale bar = 50 μm) (****$p < 0.0001$, ***$p < 0.001$, **$p < 0.01$, *$p < 0.05$).

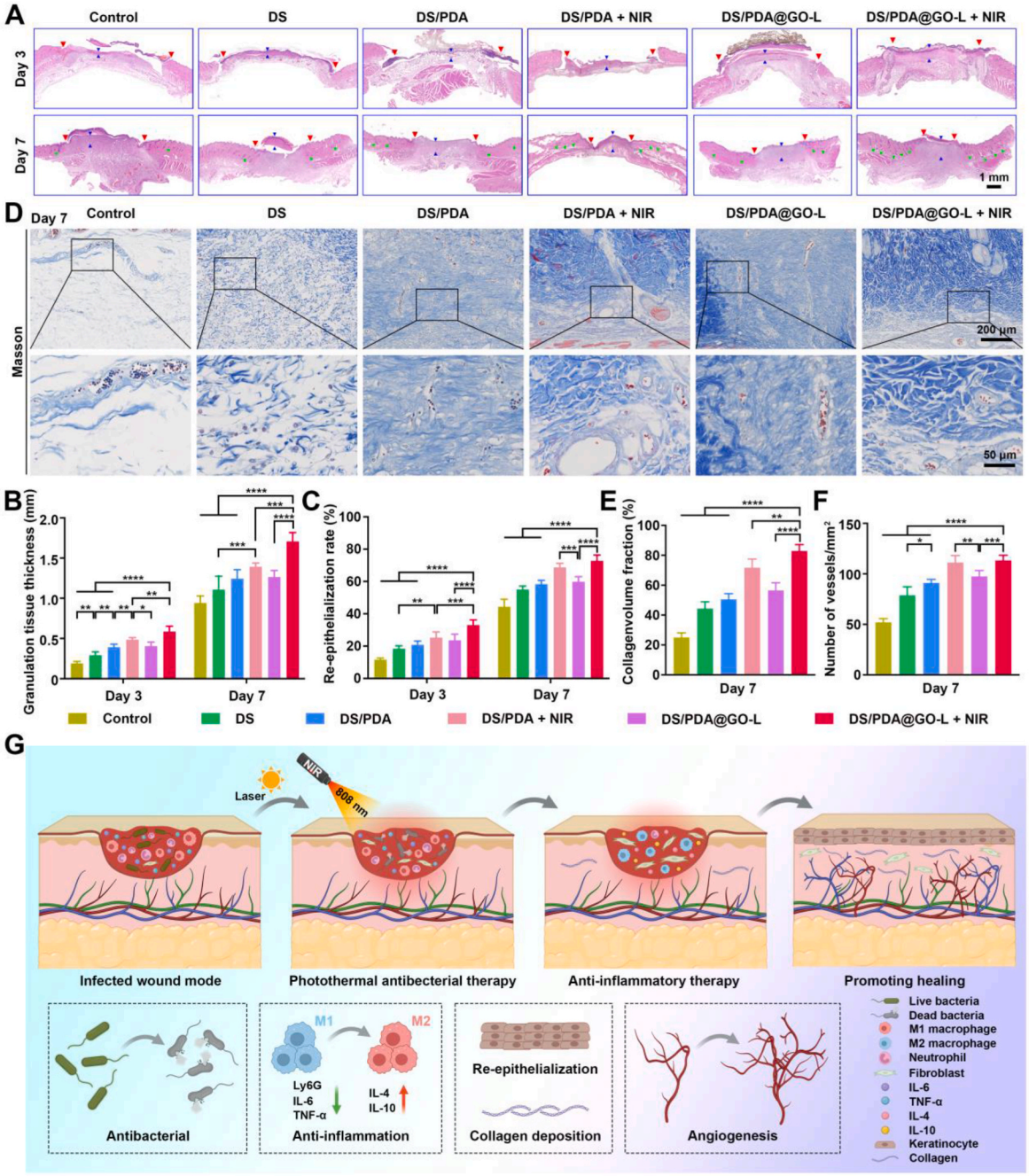

Fig. 8. Assessment of proliferative activity during healing of infected wounds. (A) H&E staining images of different treatment groups on days 3 and 7. Red arrows denote wound edges, blue arrows indicate the thickness of granulation tissue, and green arrows signify neoplastic hair follicles. (Scale bar = 1 mm) (B, C) Quantification of granulation tissue and epithelial regeneration in the wound area of the control, DS, DS/PDA, DS/PDA + NIR, DS/PDA@GO-L, and DS/PDA@GO-L + NIR groups. (D) Trichrome staining showed collagen deposition and angiogenesis in the central area of the wound in the control, DS, DS/PDA, DS/PDA + NIR, DS/PDA@GO-L, and DS/PDA@GO-L + NIR groups. (E, F) Quantification of newly deposited collagen fibers and neovascularization in the wound area of the control, DS, DS/PDA, DS/PDA + NIR, DS/PDA@GO-L, and DS/PDA@GO-L + NIR groups. (G) Schematic diagram of infected wound repair. (****p < 0.0001, ***p < 0.001, **p < 0.01, *p < 0.05).

– review & editing, Writing – original draft, Project administration. **Yongjin Fang:** Project administration, Investigation, Formal analysis. **Wenbing Wan:** Supervision, Resources, Project administration.

Ethics approval and consent to participate

All animal experiments were approved by the Animal Experiment Ethics Committee of Wenzhou Institute, University of Chinese Academy of Science in Wenzhou, China (WIUCAS24092402).

Declaration of competing interest

The authors declare no conflict of interest.

Acknowledgement

This work was financially supported by the National Natural Science Foundation of China (grant no. 82360446 & 82472403 to W. W, grant no. 82472551 to S. Chen, grant no. 82402912 to C. Cai); the Zhejiang

Provincial Natural Science Foundation of China(grant no. LR24H150001 to S. Chen); the Wenzhou Science and Technology Major Project (grant no. ZY2022026, ZY2023005 to S. Chen). The "Thousand Talents Plan" of Jiangxi Province Introduces and Trains Innovative and Entrepreneurial High-level Talents (grant no. jxsq2023201027 to W. Wan). The Key Foundation of Jiangxi Provincial Natural Science Foundation (grant no. 20242BAB26139 to W. Wan). Foundation of Health Commission of Jiangxi Province (grant no. 202210603 to W. Wan)

Appendix A. Supplementary data

Supplementary data to this article can be found online at https://doi.org/10.1016/j.bioactmat.2025.03.022.

References

[1] R.M. Klevens, et al., Estimating health care-associated infections and deaths in U.S. hospitals, 2002, Publ. Health Rep. 122 (2007) 160–166, https://doi.org/10.1177/003335490712200205.
[2] G. Taubes, The bacteria fight back, Science 321 (2008) 356–361, https://doi.org/10.1126/science.321.5887.356.
[3] H. Deng, et al., Facile and eco-friendly fabrication of polysaccharides-based nanocomposite hydrogel for photothermal treatment of wound infection, Carbohydr. Polym. 230 (2020) 115565, https://doi.org/10.1016/j.carbpol.2019.115565.
[4] Y. Sun, W. Dong, L. Sun, L. Ma, D. Shang, Insights into the membrane interaction mechanism and antibacterial properties of chensinin-1b, Biomaterials 37 (2015) 299–311, https://doi.org/10.1016/j.biomaterials.2014.10.041.
[5] M.F. Mohamed, A. Brezden, H. Mohammad, J. Chmielewski, M.N. Seleem, A short D-enantiomeric antimicrobial peptide with potent immunomodulatory and antibiofilm activity against multidrug-resistant Pseudomonas aeruginosa and Acinetobacter baumannii, Sci. Rep. 7 (2017) 6953, https://doi.org/10.1038/s41598-017-07440-0.
[6] H. Haidari, et al., Polycationic silver nanoclusters comprising nanoreservoirs of Ag(+) ions with high antimicrobial and antibiofilm activity, ACS Appl. Mater. Interfaces 14 (2022) 390–403, https://doi.org/10.1021/acsami.1c21657.
[7] Q. Xu, Z. Zheng, B. Wang, H. Mao, F. Yan, Zinc ion coordinated poly(ionic liquid) antimicrobial membranes for wound healing, ACS Appl. Mater. Interfaces 9 (2017) 14656–14664, https://doi.org/10.1021/acsami.7b01677.
[8] C. Gunawan, et al., Nanosilver targets the bacterial cell envelope: the link with generation of reactive oxygen radicals, ACS Appl. Mater. Interfaces 12 (2020) 5557–5568, https://doi.org/10.1021/acsami.9b20193.
[9] J. Wang, et al., Bacteria-triggered radical anions amplifier of pillar[5]arene/perylene diimide nanosheets with highly selective antibacterial activity, Chem. Eng. J. 444 (2022) 136620, https://doi.org/10.1016/j.cej.2022.136620.
[10] J. Lin, et al., Durably antibacterial and bacterially antiadhesive cotton fabrics coated by cationic fluorinated polymers, ACS Appl. Mater. Interfaces 10 (2018) 6124–6136, https://doi.org/10.1021/acsami.7b16235.
[11] J.E. Gestwicki, L.L. Kiessling, Inter-receptor communication through arrays of bacterial chemoreceptors, Nature 415 (2002) 81–84, https://doi.org/10.1038/415081a.
[12] R. Karmakar, State of the art of bacterial chemotaxis, J. Basic Microbiol. 61 (2021) 366–379, https://doi.org/10.1002/jobm.202000661.
[13] X. Tang, et al., Magnesium oxide-assisted dual-cross-linking bio-multifunctional hydrogels for wound repair during full-thickness skin injuries, Adv. Funct. Mater. 31 (2021) 2105718.
[14] Y. Liu, P. Bhattarai, Z. Dai, X. Chen, Photothermal therapy and photoacoustic imaging via nanotheranostics in fighting cancer, Chem. Soc. Rev. 48 (2019) 2053–2108, https://doi.org/10.1039/c8cs00618k.
[15] G. Gao, Y.W. Jiang, H.R. Jia, F.G. Wu, Near-infrared light-controllable on-demand antibiotics release using thermo-sensitive hydrogel-based drug reservoir for combating bacterial infection, Biomaterials 188 (2019) 83–95, https://doi.org/10.1016/j.biomaterials.2018.09.045.
[16] V. Alinezhad, et al., Antioxidant, hemostatic, and injectable hydrogels with photothermal antibacterial activity to accelerate full-thickness wound regeneration, New J. Chem. 48 (2024) 7761–7778.
[17] C. Mao, et al., Local photothermal/photodynamic synergistic therapy by disrupting bacterial membrane to accelerate reactive oxygen species permeation and protein leakage, ACS Appl. Mater. Interfaces 11 (2019) 17902–17914, https://doi.org/10.1021/acsami.9b05787.
[18] A.S.C. Gonçalves, C.F. Rodrigues, A.F. Moreira, I.J. Correia, Strategies to improve the photothermal capacity of gold-based nanomedicines, Acta Biomater. 116 (2020) 105–137, https://doi.org/10.1016/j.actbio.2020.09.008.
[19] J. Zhou, et al., Photothermally triggered copper payload release for cuproptosis-promoted cancer synergistic therapy, Angew Chem. Int. Ed. Engl. 62 (2023) e202213922, https://doi.org/10.1002/anie.202213922.
[20] S. Bochani, et al., Injectable antibacterial gelatin-based hydrogel incorporated with two-dimensional nanosheets for multimodal healing of bacteria-infected wounds, ACS Appl. Bio Mater. 5 (2022) 4435–4453, https://doi.org/10.1021/acsabm.2c00567.
[21] G.M. Neelgund, A.R. Oki, Influence of carbon nanotubes and graphene nanosheets on photothermal effect of hydroxyapatite, J. Colloid Interface Sci. 484 (2016) 135–145, https://doi.org/10.1016/j.jcis.2016.07.078.
[22] Y. Zhao, et al., Temperature-Sensitive lipid-coated carbon nanotubes for synergistic photothermal therapy and gene therapy, ACS Nano 15 (2021) 6517–6529, https://doi.org/10.1021/acsnano.0c08790.
[23] J. Li, et al., Erythrocyte membrane camouflaged graphene oxide for tumor-targeted photothermal-chemotherapy, Carbon 146 (2019) 660–670, https://doi.org/10.1016/j.carbon.2019.02.056.
[24] S. Liu, et al., Antibacterial activity of graphite, graphite oxide, graphene oxide, and reduced graphene oxide: membrane and oxidative stress, ACS Nano 5 (2011) 6971–6980, https://doi.org/10.1021/nn202451x.
[25] Y.Y. Xie, et al., Development and antibacterial activities of bacterial cellulose/graphene oxide-CuO nanocomposite films, Carbohydr. Polym. 229 (2020) 115456, https://doi.org/10.1016/j.carbpol.2019.115456.
[26] S. Fan, et al., Injectable and ultra-compressible shape-memory mushroom: highly aligned microtubules for ultra-fast blood absorption and hemostasis, Chem. Eng. J. 460 (2023) 140554.
[27] M. Hosseini, A. Shafiee, Engineering bioactive scaffolds for skin regeneration, Small 17 (2021) e2101384, https://doi.org/10.1002/smll.202101384.
[28] S. Chen, et al., Mesenchymal stem cell-laden, personalized 3D scaffolds with controlled structure and fiber alignment promote diabetic wound healing, Acta Biomater. 108 (2020) 153–167.
[29] G. Wang, et al., Organocatalytic asymmetric N-sulfonyl amide C-N bond activation to access axially chiral biaryl amino acids, Nat. Commun. 11 (2020) 946, https://doi.org/10.1038/s41467-020-14799-8.
[30] Z. Yuan, et al., Near-infrared light-triggered nitric-oxide-enhanced photodynamic therapy and low-temperature photothermal therapy for biofilm elimination, ACS Nano 14 (2020) 3546–3562, https://doi.org/10.1021/acsnano.9b09871.
[31] X. Zhao, et al., Preparation of photocatalytic and antibacterial MOF nanozyme used for infected diabetic wound healing, ACS Appl. Mater. Interfaces 14 (2022) 18194–18208, https://doi.org/10.1021/acsami.2c03001.
[32] K. Huang, et al., Photothermal hydrogel encapsulating intelligently bacteria-capturing bio-MOF for infectious wound healing, ACS Nano 16 (2022) 19491–19508, https://doi.org/10.1021/acsnano.2c09593.
[33] M. Ebrahimi Naghani, M. Neghabi, M. Zadsar, H. Abbastabar Ahangar, Synthesis and characterization of linear/nonlinear optical properties of graphene oxide and reduced graphene oxide-based zinc oxide nanocomposite, Sci. Rep. 13 (2023) 1496.
[34] Y. Gong, et al., Exudate absorbing and antimicrobial hydrogel integrated with multifunctional curcumin-loaded magnesium polyphenol network for facilitating burn wound healing, ACS Nano 17 (2023) 22355–22370.
[35] K. Yang, et al., Low temperature photothermal therapy: advances and perspectives, Coord. Chem. Rev. 454 (2022) 214330.
[36] D. Hu, et al., Indocyanine green-loaded polydopamine-reduced graphene oxide nanocomposites with amplifying photoacoustic and photothermal effects for cancer theranostics, Theranostics 6 (2016) 1043.
[37] Y. Zhao, et al., Smart trap-capture-kill antibacterial system for infected microenvironment improvement and vascularized bone regeneration via magnetic thermotherapy, Adv. Funct. Mater. 33 (2023) 2214734.
[38] J. Yang, et al., Self-assembled biofunctionalized chitosan-derived nanocomposite for long-lasting antibacterial packaging at room temperature, ACS Sustain. Chem. Eng. 12 (2023) 561–571.
[39] X. Chen, et al., A one-step polyphenol-based functionalization strategy of dual-enhanced antibacterial and osteogenic surfaces, Chem. Eng. J. 490 (2024) 151792.
[40] S. Khunmanee, et al., Effective wound healing on diabetic mice by adhesive antibacterial GNPs-lysine composited hydrogel, iScience 27 (2024).
[41] L. Xiao, et al., A 3D chemotactic-thermo-promo bacterial hunting system: programmatic bacterial attract, capture, killing and healing the wound, Chem. Eng. J. 417 (2021) 128123.
[42] Y. Bai, et al., Spatial modulation of individual behaviors enables an ordered structure of diverse phenotypes during bacterial group migration, Elife 10 (2021) e67316.
[43] A. Jaggessar, H. Shahali, A. Mathew, P.K.D.V. Yarlagadda, Bio-mimicking nano and micro-structured surface fabrication for antibacterial properties in medical implants, J. Nanobiotechnol. 15 (2017) 1–20.
[44] S. Khalid, A. Gao, G. Wang, P.K. Chu, H. Wang, Tuning surface topographies on biomaterials to control bacterial infection, Biomater. Sci. 8 (2020) 6840–6857.